Ann. occup. Hyg., Vol. 49, No. 1, pp. 1–15, 2005

Published by Oxford University Press
doi:10.1093/annhyg/meh065

Aerodynamic Characteristics and Design Guidelines of Push–Pull Ventilation Systems

R. F. HUANG[1]*, S. Y. LIN[1], S.-Y. JAN[1], R. H. HSIEH[2], Y.-K. CHEN[3], C.-W. CHEN[4], W.-Y. YEH[4], C.-P. CHANG[4], T.-S. SHIH[4] and C.-C. CHEN[5]

[1]Department of Mechanical Engineering, National Taiwan University of Science and Technology, 43 Keelung Road, Section 4, Taipei, Taiwan, PRC; [2]Department of Mechanical Engineering, Kuan Wu Institute of Technology, 151 Yide St., Beitou Chiu, Taipei, Taiwan 112, PRC; [3]Department of Occupational Safety and Health, Chang Jung Christian University, Kway Jen, Taiwan, PRC; [4]Institute of Occupational Safety and Health, Council of Labor Affairs, No. 99, Lane 407, Hengke Rd., Shijr City, Taipei, Taiwan, PRC; [5]Institute of Occupational Medicine and Industrial Hygiene, National Taiwan University, 1 Jen-Ai Rd., Sec. 1, Taipei, Taiwan, PRC

Received 19 May 2004; in final form 12 July 2004; published online 9 December 2004

Aerodynamic characteristics such as the flow patterns, velocity field, streamline evolutions, characteristic flow modes and characteristic flow regimes of the push–pull ventilation system are cross-examined by using the laser-light sheet smoked-flow visualization method and laser Doppler velocimetry. Four characteristic flow modes, which are denoted as *dispersion*, *transition*, *encapsulation* and *strong suction*, are identified in the domain of the push-jet and pull-flow velocities at various open-surface tank widths and rising gas velocities. It is argued phenomenologically, from the aerodynamic point of view, that operating the system in the *strong suction* regime would be a better strategy than operating it in other characteristic regimes for the consideration of capture efficiency. Design guidelines are developed and summarized based on the results obtained from this study. The regression formulas for calculating the critical values of the push-jet and the pull-flow velocities are provided for easy access. The sulfur hexafluoride tracer gas validation technique is performed to measure the capture efficiency. The results of tracer gas validations are consistent with those obtained from the aerodynamic visualization and measurements. The operation points obtained by employing the American Conference of Governmental Industrial Hygienists design criteria are compared with the results obtained in this study for both the aerodynamics and the capture efficiency. Methods for improving the capture efficiency and energy consumptions are suggested.

Keywords: aerodynamic characteristics; push–pull ventilation; tracer gas

NOMENCLATURE

A_g	area of open-surface tank ($=H \times L$)
$C_{o,g}$	concentration of sulfur hexafluoride gas measured at 0.5 m upstream of end-opening of exhaust pipe when sulfur hexafluoride gas is injected into pull hood
$C_{o,s}$	concentration of sulfur hexafluoride gas measured at 0.5 m upstream of end-opening of exhaust pipe when sulfur hexafluoride gas is released with air from open-surface tank
D	height of pull hood
E	height of push nozzle
H	width of open-surface tank
L	transverse length of open-surface tank
Q_b	blowing volumetric flow rate of push nozzle
Q_g	volumetric flow rate through open-surface tank
Q_s	suction volumetric flow rate of pull hood
U	distance between lower edge of push nozzle/pull hood and liquid-surface-simulating screen of open-surface tank
u	local velocity component in x direction
v	local velocity component in y direction
v_b	area-averaged flow velocity of push jet at exit of push nozzle ($=Q_b/(E \times L)$)
v_b^*	push-jet velocity at minimum energy consumption point

*Author to whom correspondence should be addressed.
Tel: +886-2-2737-6488; fax: +886-2-2737-6460;
e-mail: rfhuang@mail.ntust.edu.tw

v_g area-averaged rising gas velocity at exit of open-surface tank ($Q_g/(H \times L)$)
v_g^* pull-flow velocity at minimum energy consumption point
v_s area-averaged flow velocity of pull flow at inlet of pull hood ($=Q_s/(D \times L)$)
S slope ($\equiv v_s/v_b$) of *critical operation boundaries* at $v_b > v_b^*$
W height of push-hood flange
x coordinate along the direction of push jet that originated at the bottom edge of push nozzle in a symmetry plane
y coordinate along the direction in height of push nozzle that originated at the bottom edge of push nozzle in a symmetry plane
z coordinate along the direction in length of push nozzle that originated at bottom edge of push nozzle in a symmetry plane
η capture efficiency of hood ($=C_{o,g}/C_{o,s}$)
V kinematic viscosity of air

INTRODUCTION

Pull hoods combined with push airflows have been widely applied in the industries that require the removal of contaminant vapors, fumes or aerosols from a large open surface during the half-century since Malin (1945) reported that a push–pull system can save airflow by about 50% when compared with using side exhaust alone.

Many investigators have studied the key parameters. Since the 24th edition of the ACGIH (2001) ventilation guide, Rota *et al*. (2001) have employed a numerical method to calculate the time-averaged flow field and have recommended some rules based on the calculated streamline patterns for the design of the push–pull system, and Marzal *et al*. published a series of papers (2002a,b,c, 2003a,b) on the development of an analytical model for the evaluation, determination and interpretation of capture efficiencies, influence of push-nozzle geometry on capture efficiency, methodologies for determining capture efficiencies and flow visualization results in the experimentally simulated surface-treatment tanks. Mathematical models and flow patterns on the open surface were addressed and discussed.

Most of the recommended design guidelines in the literature were based on the experimental results of tracer gas concentration measurements together with empirical rules for tunable parameters. There is still need for more study in the flow physics that governs the transport process of the contaminants, the push flows and the environmental air through the pull hood, and design strategy based on the flow physics is also a field where more effort is required. In this work, in order to understand the inter-correlation among the primary design parameters of the push-flow velocity, pull-flow velocity, rising gas velocity and open-surface width, and to obtain design guidelines based on detailed aerodynamic characteristics of the flow field, a series of studies were conducted in an experimentally simulated open-surface tank. The laser-light sheet flow visualization technique and a laser Doppler anemometer were applied to diagnose and analyze the physics embedded in the complex flows. A design procedure based on the systematic diagnostic results of the flow field is proposed. The SF_6 tracer gas detection technique was subsequently used to evaluate the overall capture efficiency and local dispersion concentration and to validate the proposed design guidelines.

EXPERIMENTS

Test rig

The system consists of three parts—the push nozzle, the pull hood and the open-surface tank, which is made of plexiglas and arranged as shown in Fig. 1. The coordinate system, the geometric parameters of the system and the flow parameters are defined in Fig. 2. The open-surface tank has a transverse length $L = 0.5$ m in the z direction. The width H of the open-surface tank is skillfully designed so that it can be easily varied between 0.5 and 1.5 m without causing any leakage of gas. We demonstrate in the Results and Discussion section that the governing principles, which dominate the embedded physics, are similar in either a short or a long tank if the aerodynamic phenomena are considered. We also demonstrate that using the lateral exhaust hood on a short-length tank does not result in better performance than using the push–pull system. The push–pull system is not installed on the longer side of the tank in our experimental system because the flow is basically two-dimensional in the symmetry plane and this arrangement of the experimental set-up can save expenditure. When using the design method proposed in this article for practical application, most of the push–pull system should be installed on the longer side of the tank if the spatial occupation is convenient for installation of the ducts, fans/blowers and nozzle/hood.

The open-surface tank is in reality a large rectangular nozzle, where the airflows used to simulate the rising gas are driven by a centrifugal fan. The airflows go through a venturi flow meter, a series of flow conditioning devices (including a buffer tank, four flow distribution conduits, a perforated plate, a nozzle section, honeycombs and several layers of mesh screens) to reduce the turbulence and increase the flow uniformity, and a layer of liquid-surface-simulating screen, and then vent up to the atmosphere. The liquid-surface-simulating screen is made of fine metal grids with a mesh-size to wire-diameter

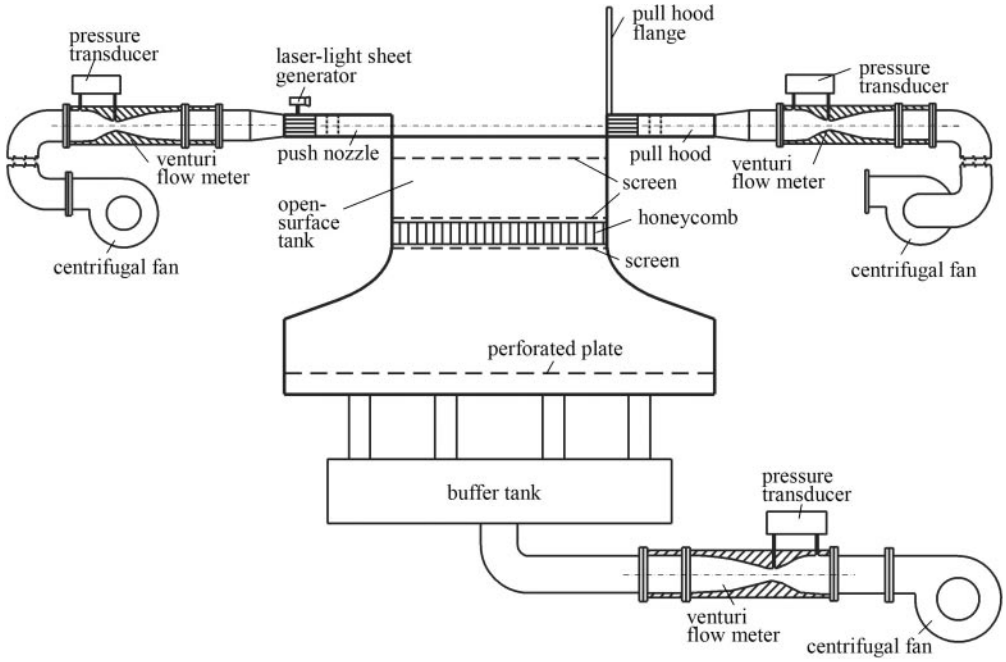

Fig. 1. Experimental setup.

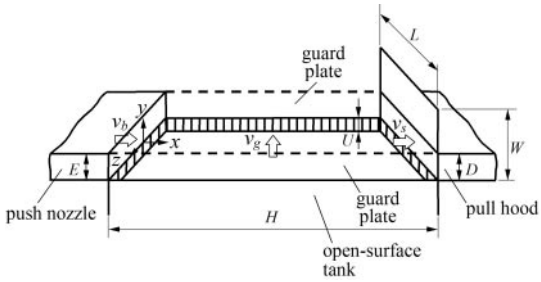

Fig. 2. Definitions of geometric parameters.

ratio of about 2. The rising velocity of the air on the open surface was tested at 15 evenly distributed points using a calibrated fine-wire hot-wire anemometer. The results showed that the non-uniformity of the rising air velocity distributions is less than 1.5%.

Both the push nozzle and the pull hood have a rectangular cross-section with a cross-stream length $L = 0.5$ m, which is the same as that of the open-surface tank. The axes of the push and pull devices are arranged vertically to the axis of the open-surface tank. The distance between the lower surface of the push nozzle/pull hood and the liquid-surface-simulating screen of the open-surface tank, U, is 0.1 m. The push-nozzle height, E, is the same as the pull-hood height D with a fixed value of 0.05 m. Smaller push-nozzle heights are also tested in this study. Although the data are not shown because it is not the primary focus of this paper, the effects of the push- and the pull-hood heights are stated in the Design Guidelines section below. Honeycombs are inserted into the push nozzle and the pull hood to improve the uniformity of the jet velocity at the exit of the push nozzle and the suction flow at the opening of the suction hood. The uniformities of the jet and the suction flow are surveyed by a fine-wire hot-wire anemometer. The results show that the maximum non-uniformity of the jet and the suction flow are lower than 2%. The push jet and the suction flow are driven separately by two centrifugal fans. Venturi flow meters are used to measure the flow rates through the push nozzle and the pull hood. A pull-hood flange with a height $W = 0.5$ m is installed, while the push nozzle is not equipped with a flange. Determination of the subsidiary parameters U and W are made according to the experimental results of Shibata *et al*. (1982a,b), which show that when $U/E \geqslant 2$ and $W/E \geqslant 5$ the geometries of the liquid-surface height and the pull-flange height would have negligible effect on the flow patterns.

The flow parameters include the push-jet velocity v_b (the area-averaged blowing velocity at the exit of the push nozzle), the pull-flow velocity v_s (the area-averaged suction velocity at the opening of the pull hood) and the rising air velocity v_g (the area-averaged gas velocity at the plane of $y = 0$). The width of the open-surface tank, H, together with the flow parameters, v_b, v_s and v_g, are the primary influencing factors in this work. The values of v_b, v_s and v_g are

varied in the ranges of 0–3.5, 0–16 and 0–0.2 m/s, respectively.

Laser-light sheet flow visualization

The laser beam provided by a 5 W argon-ion laser is transmitted through an optical fiber and connected to a 20° laser-light sheet expander. The laser-light sheet expander is mounted on an adjustable block so that the light sheet can be flexibly aimed at any target plane. In this study, the light sheet is aligned across the symmetry plane of $z = 0$. The laser-light sheet has a thickness of ~0.5 mm. Mineral oil mist is continuously seeded through a homemade smoke generator into the conduit of the push nozzle and vented out with the push-jet flow to scatter the laser light. The diameter of the oil-mist particles, measured by a Malvern 2600C particle analyzer, is 1.7 ± 0.2 μm. The density is 0.821 g/ml. Ignoring the effect of turbulent diffusion, the relaxation time constant is estimated to be $<7.7 \times 10^{-5}$ s and the Stokes number is in the order of 10^{-6} within the range of experiment. Therefore, the seeding particles can properly follow the flow fluctuations at least up to 10 kHz (Flagan and Seinfeld, 1988). The particle images are recorded by both a Minolta Dynax 9xi still camera and a Hi-8 CCD camera. The still camera is equipped with an asynchronous variable electronic shutter, ranging from 1/12 000 to 30 s. The Hi-8 CCD camera can record images at 30 fps.

Laser Doppler velocimeter

The velocity field is measured with a two-component laser Doppler velocimeter. The whole-spectrum laser-light beam is provided by a 5 W argon-ion laser. Two color filters are used to allow blue and green laser beams of 514.5 and 488 nm, respectively, to pass through. They are subsequently split and focused through an optical system. The dimensions of measuring volumes of the green and blue components are $0.075 \times 0.075 \times 0.680$ and $0.071 \times 0.071 \times 0.645$ mm, respectively. The fringe separations of the green and blue components are 2.34 and 2.22 μm, respectively. The system is configured for backward scattering and installed with a Bragg cell and two electronic frequency shifters for the detection of direction ambiguity. Two electronic correlators are used to process the frequency of the signals. The digital outputs of the correlation processors are fed into a data-acquisition system. Each velocity data record consists of 1000 samples, about 3 s long. Uncertainty of the velocity measurements is estimated to be less than ±0.5% of reading. The seeding particles are the same as those used in the flow visualization.

Sulfur hexafluoride (SF_6) detector

In the tracer gas experiment, a Miran 1 BX Portable Ambient Air Analyzer is used to measure the concentration of the sulfur hexafluoride gas. The Miran 1BX Portable Ambient Air Analyzer is a single-beam infrared spectrometer, using a pyroelectric lithium tantalite substrate as the detector that can detect concentrations of 150 toxic gases or vapors. The flow rate of pump for proper operation is 25–30 l/min. Sampling goes through a probe of a filter enclosure. The sampled gas is drawn through a hose and directed into a gas cell. The sample gas absorbs infrared energy from the infrared beam. The amount of absorption is measured by the detector, and subsequently amplified and converted to concentration units by the electronics. For SF_6 concentration measurement, the span is from 0 to 99 999 ppm. After being calibrated in the range of 0–500 ppm, the accuracy of measurement is ±5% of reading. The lower limit of measurement is 0.6 ppm. *In situ* calibration was done each time, before the experiment was conducted.

RESULTS AND DISCUSSION

Gas transport process and aerodynamic characteristics

Characteristic flow modes. By using the laser-light sheet flow visualization technique with the assistance of smoke particles as the light-scattering media, the flow patterns in the symmetry plane are observed. Figures 3 and 4 show four fundamental flow patterns observed at different values of the pull-flow velocity v_s when the push-jet velocity v_b and the rising air velocity v_g are set at 0.3 and 0.05 m/s, respectively. In Fig. 3 the smoke mists are issued along with the push-nozzle flow. While in Fig. 4, the smoke particles are issued along with the rising air flow from the open-surface tank.

In Fig. 3a where the pull-flow velocity is low, the push-jet going out of the push nozzle is tilted up by an angle by the rising current from the open-surface tank. After about the midpoint of the width of the open-surface tank, influence of the pull velocity becomes appreciable so that a small part of the jet flow is drawn down and goes into the pull-hood opening, while a large part of the jet flow disperses and goes across the upper edge of the pull-hood flange, because the pull velocity is not high enough. Along the jet boundary, the coherent structures (the vortices) are evolved because of the concentration of the vorticity that is induced by the shear effect developed in between the jet and the environmental flows (Tritton, 1988). During the evolution process of these coherent structures, some of the atmospheric air above the jet and the airflow under the jet, which is rising from the open-surface tank, are entrained into the jet by the rolling-and-traveling motions of the vortices. The coherent structures entrain neighboring air and the mixedness increases as the jet

evolves downstream. When a large part of the jet fluids is dispersed into the atmosphere, as shown in Fig. 3a, the airflow issued from the open-surface tank and entrained by the coherent structures is inevitably dispersed into the atmosphere along with the jet fluid. This phenomenon can be seen clearly in Fig. 4a where the smoke particles released along with the rising air from the open-surface tank escape apparently to the atmosphere instead of being blocked under the bowed jet trajectory. This type of flows usually occurs at low-pull velocity v_s and is called the *dispersion* mode. Operating a push–pull ventilation system at this mode would result in a serious dispersion of a large quantity of the rising contaminants from the open-surface tank to the atmosphere. A large push-jet velocity may cause such a condition if the corresponding suction strength developed by the pullhood is not properly matched.

In Fig. 3b, the pull velocity v_s is greater than that of Fig. 3a. The highest point of the bowed jet trajectory moves to a location about three-quarters of the tank width from the push-nozzle tip. A large part of the jet fluids and the entrained environmental fluids are drawn into the pull-hood opening. A small part of the jet fluids goes up to a high level above the pull-hood along the pull-hood flange, detaches from the flange, turns around towards the jet, and is finally drawn by the suction hood. The air issued from the open-surface tank, as presented in Fig. 4b, is dispersed up to a high level due to the entrainment effect of the jet-evolution process and is finally sucked into the pull hood. Although not clear enough in the picture, it is observable *in situ* and from the continuous video images that some of the smokes issued from the open-surface tank recirculate around the area near the flange and above the pull-hood opening. This type of flow, which is called the *transition* mode, usually occurs at pull velocity v_s higher than that of the *dispersion* mode.

At further higher suction velocity v_s, the jet is still tilted up by the rising air from the open-surface tank, as shown in Fig. 3c. The tilt angle, however, is not as large as that found in the *transition* mode. Also, all of the jet fluids and the entrained environmental airs are drawn into the pull-hood opening. It seems that all the rising contaminants are isolated under the jet, as shown in Fig. 3c. However, traces of the smoke issued from the open-surface tank presented in Fig. 4c show that although all the smokes are finally drawn into the pull hood, the risk of turbulent and molecular dispersions across the jet to the atmosphere during the evolution process from the push-nozzle tip to the pull-hood opening is significant. Flows with this type of pattern are called the *encapsulation* mode.

When the suction velocity v_s is increased further, the trajectory of the jet remains almost horizontal or

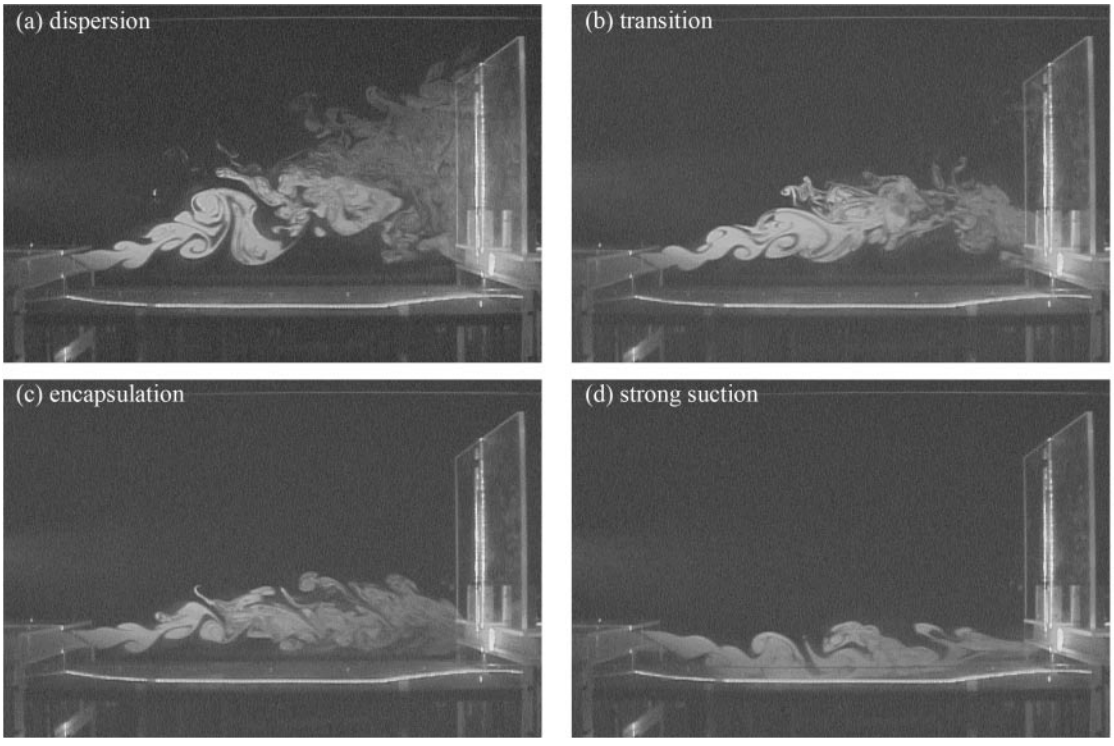

Fig. 3. Photos of typical characteristic flow modes obtained by using smoked-flow visualization method assisted with laser-light sheet scattering. Smoke released with push-jet flow. $v_g = 0.05$ m/s, $v_b = 0.30$ m/s. (a) $v_s = 1.55$ m/s, *dispersion* mode; (b) $v_s = 2.79$ m/s, *transition* mode; (c) $v_s = 3.49$ m/s, *encapsulation* mode; (d) $v_s = 4.17$ m/s, *strong suction* mode. Shutter speed 1/30 s.

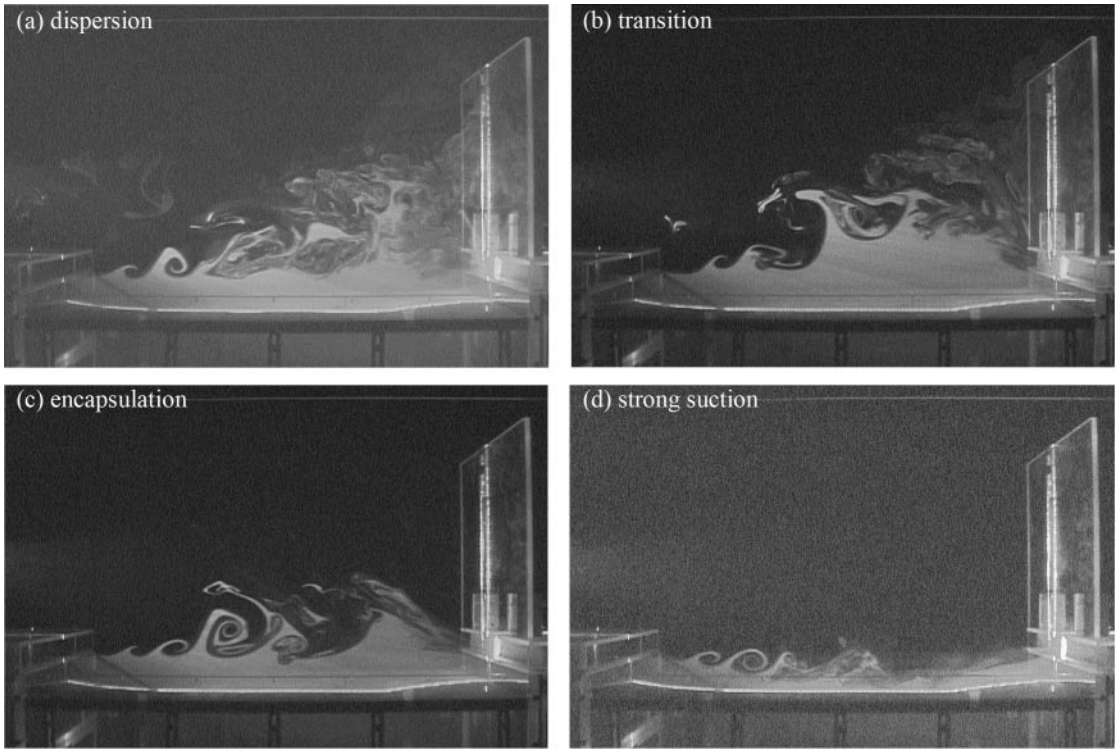

Fig. 4. Photos of typical characteristic flow modes obtained by using smoked-flow visualization method assisted with laser-light sheet scattering. Smoke released with rising air from open-surface tank. $v_g = 0.05$ m/s, $v_b = 0.30$ m/s. (a) $v_s = 1.72$ m/s, *dispersion* mode; (b) $v_s = 2.49$ m/s, *transition* mode; (c) $v_s = 2.83$ m/s, *encapsulation* mode; (d) $v_s = 4.30$ m/s, *strong suction* mode. Shutter speed 1/30 s.

even bowed toward the screen installed in the tank, as shown in Fig. 3d. The tendency of bowing down of the jet is possibly induced by the Coanda effect (Newman, 1961) when the jet momentum, as well as the distance between the jet and the wall, are matched in a proper range. Under this circumstance, the smoke particles issued from the open-surface tank are all drawn into the pull hood and isolated by the jet, as shown in Fig. 4d. The risk of dispersion of the tank fluids to the upper atmosphere across the jet due to the entrainment by the coherent structures is relatively low. Flows of this type of pattern are called the *strong suction* mode. If the push–pull ventilation system is operated in this characteristic mode, escape of the pollutants coming from the open-surface tank should be less than that operating at other characteristic modes. Besides, because the whole air curtain generated by the push and pull flows in the *strong suction* mode is below the level of the upper edges of the push–pull slots, it is possible to avoid the pollutants coming out of the width-sides of the open-surface tank by simply installing guard-plates along the sides of the open-surface tank.

Hand sketches shown in Fig. 5 summarize the observed typical flow patterns. There are three typical flow patterns included in the *dispersion* mode. The flow pattern (c) of the *dispersion* mode is the one corresponding to Figs 3a and 4b, which is usually observed at large push-jet velocities. The flow pattern shown in the subset (a) of the *dispersion* mode occurs when the push-jet velocity is extremely low. Under this situation the issued jet is pushed up by the rising air from the open-surface tank and rolls back towards the upstream area. The flow pattern shown in the subset (b) of the *dispersion* mode appears when the velocity of the push jet is in between those of pattern (a) and pattern (c). Under this situation, the strengths of the push jet and the pull sink are both insufficient because of which the rising air emitted from the open-surface tank 'breaks through' the air curtain and escapes to the atmosphere. There are also three typical flow patterns included in the *transition* mode. The flow pattern (c) of the *transition* mode is the one corresponding to Figs 3b and 4b, which is usually observed at large push-jet velocities. The flow patterns shown in subsets (a) and (b) of the *transition* mode are found at push-flow velocities lower than that for subset (c). The hand sketches shown for the *encapsulation* and *strong suction* modes in Fig. 5 delineate the flow patterns discussed in Figs 3c and 4c and in Figs 3d and 4d, respectively.

Velocity field. The velocity vectors and the streamline patterns of different characteristic flow modes in

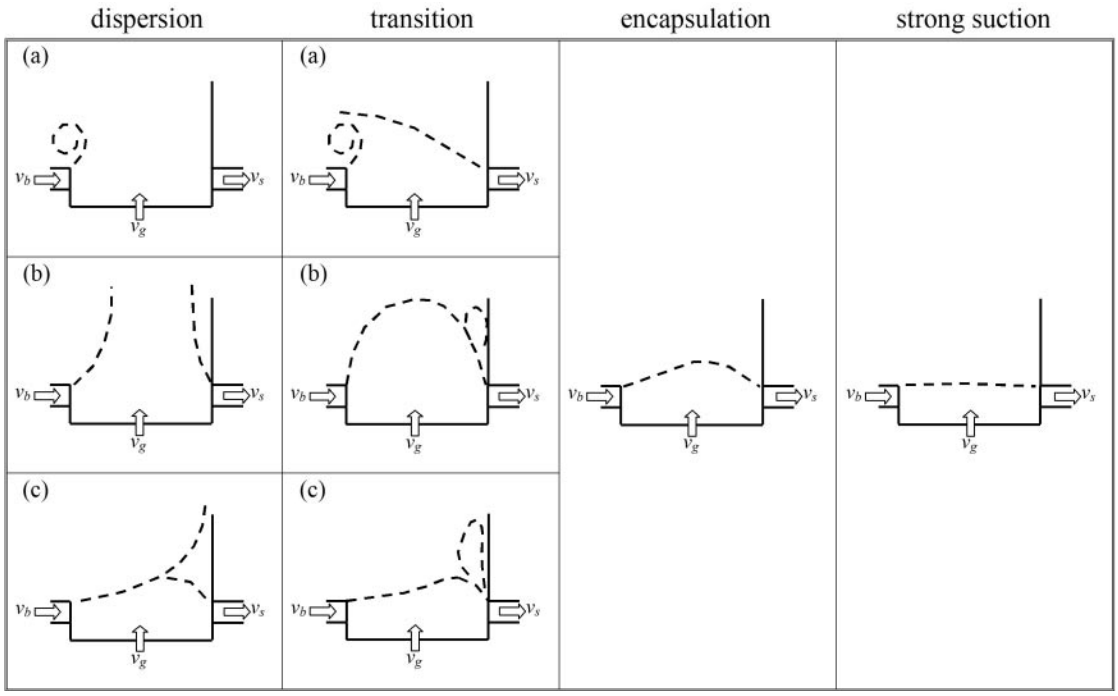

Fig. 5. Hand sketches delineating flow patterns of typical characteristic flow modes.

the symmetry plane at $H = 1$ m are superimposed onto the corresponding long-exposed pictures of smoke-flow patterns, as shown in Fig. 6. The velocity data are obtained by LDV measurements. The streamlines are obtained by using the shooting method based on the velocity vectors.

In Fig. 6a for the *dispersion* mode, the suction strength of the pull hood is weak so that the rising air released from the open-surface tank pushes the jet issued from the push nozzle up and therefore forms a hump in the streamline that evolves from the bottom edge of the push nozzle $(x, y) = 0$. The boundary of the hump coincides almost with the lower boundary of the traces of the smoked jet. The existence of this boundary does not imply that the rising gas from the tank is isolated by the lower boundary of the deflected jet because the streamline and smoke patterns shown here are time-averaged ones. The dynamic behaviors of the flows discussed in the previous section clearly show the entrainment mechanism developed by the evolving vortices. Above the hump, the smoke particles disperse up to a wide region. On the pull-hood flange, the streamlines form a stagnation point at $y/D \approx 5$. Above the stagnation point, the streamlines turn upwards along the flange and eventually vent out to the atmosphere. Below the stagnation point, the streamlines turn downward and eventually go into the suction hood. The streamlines going across the upper boundary of the jet indicates the entrainment of the atmospheric air by the deflected jet. In Fig. 6b for the *transition* mode, the hump appearing in Fig. 6a becomes insignificant. Also, the stagnation point on the flange disappears. Although all the streamlines near the flange above the upper edge of suction hood go to the suction opening, traces of the dispersed smoke can still be seen around that region. In Fig. 6c and 6d for the *encapsulation* and *strong suction* modes, the boundaries of the hump appearing in Fig. 6a and 6b become concave downwards. In Fig. 6d a recirculation bubble is formed in the area near and below the push nozzle. Apparently, it is difficult to identify the dynamic characteristic flow behaviors in this case from the time-averaged streamline patterns obtained from LDV measurements, because the entrainment, dispersion and transportation processes of the fluids induced by the complex interaction among the push jet, suction stream and the rising air are unsteady phenomena. From the fundamental principle of the fluid mechanics, the smoke particles in the pictures delineate the streaklines of the flows. The streaklines, however, would not coincide with the streamlines if the flow is unsteady. Therefore, the flow patterns delineated by the time-averaged flow-velocity measurements using the LDV or Pitot tube may not provide significant contributions to the diagnostics of dispersion characteristics of the unsteady flows.

Figure 7 shows the distributions of the axial velocity component u of four characteristic flow modes along the geometric centerline $y/D = 0.5$ at a fixed v_b.

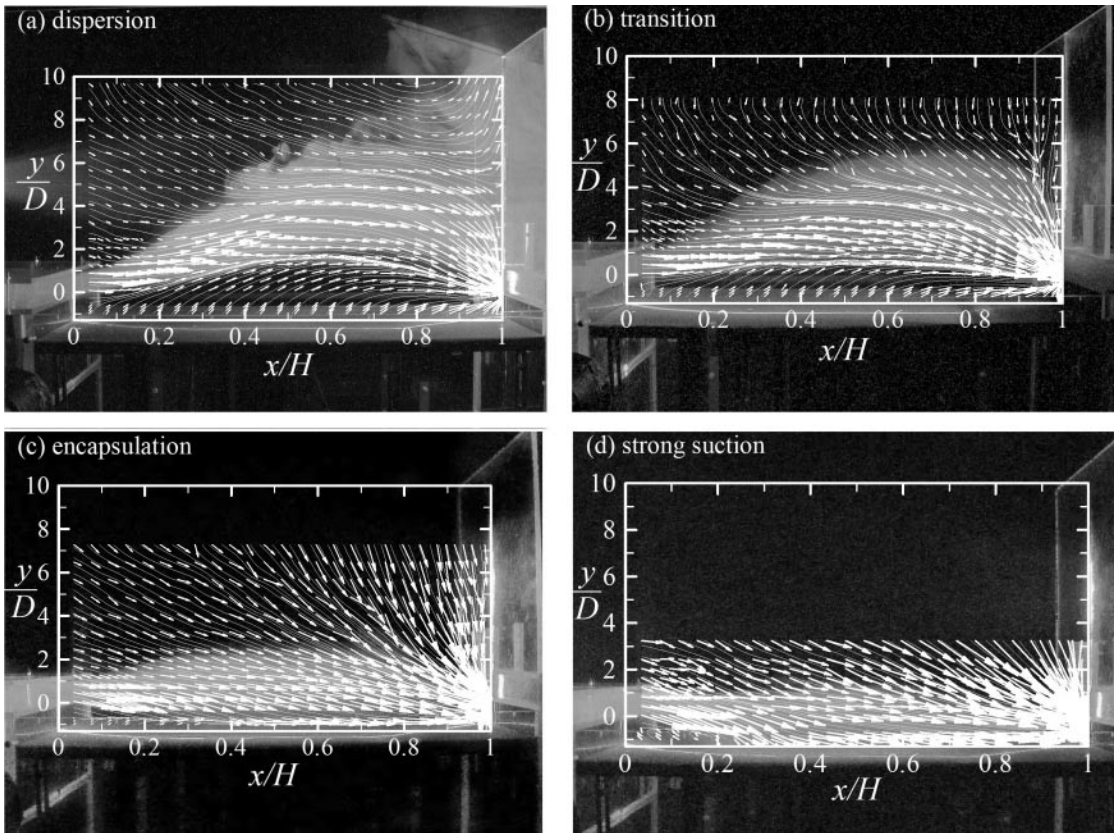

Fig. 6. Velocity vector field and corresponding streamline patterns of typical characteristic flow modes superimposed onto long-exposed smoke flow patterns. Exposure time of smoke pattern is 4 s. $H = 1.0$ m, $v_g = 0.05$ m/s, $v_b = 0.3$ m/s. (a) $v_s = 1.48$ m/s, *dispersion* mode; (b) $v_s = 2.0$ m/s, *transition* mode; (c) $v_s = 3.6$ m/s, *encapsulation* mode; (d) $v_s = 5.0$ m/s, *strong suction* mode.

These velocity profiles indicate two features. First, for the *dispersion* and *transition* modes, the suction velocity v_s is not high enough so that the axial centerline velocities near the push nozzle ($x/H < 0.1$) are not significantly affected. In the region of $0.1 < x/H < 0.2$, the velocity profiles drop sharply. Second, in the *encapsulation* and *strong suction* modes, the influences of the suction force on the axial centerline velocities are extended upstream to the push-nozzle tip. For the *encapsulation* mode, the values of u/v_s remain almost constant downstream until $x/H \approx 0.7$. In the region of $x/H > 0.7$, the velocity profile is sharply pulled up by the suction force provided by the pull hood. The distribution of the axial centerline velocities of the *strong suction* mode behaves similarly to that of the *encapsulation* mode except that the velocity profile of the *strong suction* mode is concave downwards. These two features in the centerline velocity distributions may be used for the diagnostics of the characteristic flow modes if a quantitative index is required. However, the smoke-flow visualization method assisted by the laser-light sheet technique may be a more convenient and rapid way for identification of the flow features.

Characteristic flow regimes. Figure 8 shows the characteristic flow regimes where the above-discussed characteristic flow modes are observed at $H = 1.5$ m. The bands of short slashed lines represent boundaries between different characteristic flow modes. They are obtained by fixing the push-jet velocity at various values and increasing the pull-flow velocity gradually from zero to high values. The characteristic flow modes are identified according to cross-reference of the *in situ* visual-flow patterns, the pictures and the video motion images. The thickness of the slash-lined boundary bands indicates the uncertainty of identification. Figures of the characteristic flow regimes for the open-surface tank width other than 1.5 m are also obtained, although not shown here. They all have similar patterns and characteristics.

All the boundaries between the characteristic flow regimes follow similar general behaviors, although the critical values of (v_b, v_s) are different for different v_gs, as shown in Fig. 8a–d. When the boundaries in Fig. 8a–d are compared with each other, it is apparent that the larger the value of v_g is, the higher the value of critical v_s will be for the same value of v_b. The critical

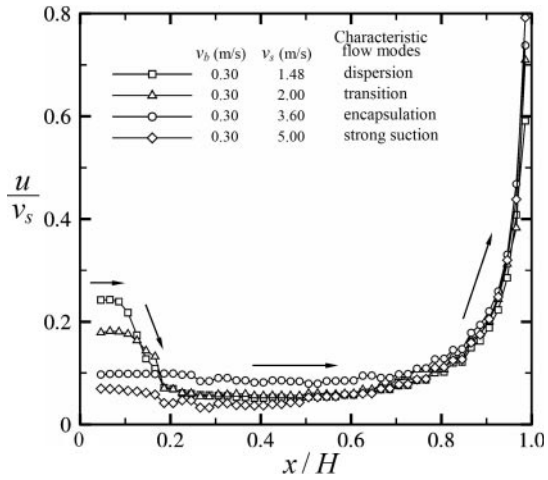

Fig. 7. Axial velocity distributions of four characteristic flow modes along x direction in geometric centerline at $y/D = 0.5$ at $v_g = 0.05$ m/s and $H = 1.0$ m.

pull-flow velocity v_s on the boundaries decreases first with the increase of the push-jet velocity v_b when v_b is increased a little from zero. The tendency of the decrease of the pull-flow velocity benefits from the push jet. When the push-jet velocity v_b is increased to a value that is commonly lower than about 0.3 m/s, the corresponding critical value of v_s reaches a minimum. When the push-jet velocity v_b is further increased beyond the minimum critical value, the corresponding critical value of v_s increases. The increase rate can be taken as approximately linear.

As discussed previously, according to the aerodynamic behaviors of the flow field shown in Figs 3 and 4, the push–pull ventilation system may attain a good performance if the operation parameters of v_b and v_s are set in the *strong suction* regime for the corresponding v_g and H. Therefore, the boundary between the regimes of the *encapsulation* and the *strong suction* mode becomes the minimum operation requirement. That boundary is hereafter termed the *critical operation boundary* and the minimum point on this boundary is called the *minimum energy-consumption point*, as shown in Fig. 6. The values of (v_b, v_s) corresponding to the *minimum energy-consumption point* are denoted by (v_b^*, v_s^*). It is obvious from Fig. 8 that a small velocity v_b together with a proper value of v_s would be enough to force the 'air curtain' to the *strong suction* regime. If the push-jet velocity v_b is set at a high value, the pull-flow velocity v_s will have to be correspondingly large to operate in the *strong suction* regime. In our experience, if the cross draft in the environment is not significant, it is recommended not to use high push-jet velocity if the energy-saving is taken into account. The primary design work by employing the aerodynamic observations, therefore, requires determination of the functional relationship among the parameters of v_b, v_s, v_g, and H on the *critical operation boundary*.

Discussion on ACGIH design code

According to the ACGIH design code (ACGIH, 2001), the criteria for determination of the push- and pull-flow rates are listed as follows (the units have been converted into metric system).

The push-flow rate Q_b can be calculated by

$$Q_b = 40.9 \times L \times E^{0.5} \quad (1)$$

where Q_b is the blowing volumetric flow rate of the push nozzle in cubic meters per minute, and L and E are the width and height of the push nozzle, respectively, in meter, as shown in Fig. 2.

The pull-flow rate Q_s can be calculated by

$$Q_s = 22.9 \times A_g \quad \text{for } T_g < 65.5°C \quad (2)$$

$$Q_s = \left(0.22 \times T_g + 8.44\right) \times A_g \quad \text{for } T_g > 65.5°C \quad (3)$$

where Q_s is the suction volumetric flow rate of the pull hood in cubic meter per minute, A_g is the area of the open-surface tank ($\equiv L \times H$) in square meter, and T_g is the temperature of the liquid surface in °C.

By plugging the geometric parameters (H = 0.5–1.5 m, L = 0.5 m, E = 0.05 m) used in this study in equations (1)–(3), calculating for two cases: $T_g < 65.5°C$ and $T_g = 100°C$, and converting the volumetric flow rates Q_b and Q_s into the push velocity v_b and pull velocity v_s, the results by employing the ACGIH design code are obtained and listed in Table 1. Since the dimensions of the push nozzle are fixed in all cases, the push-jet velocities v_b for $H = 0.5$, 1.0 and 1.5 m have the same value of 3.1 m/s. The pull-flow velocities v_s for $H = 0.5$, 1.0 and 1.5 m are 3.82, 7.63 and 11.45 m/s, respectively, for $T_g < 65.5°C$. They are 5.07, 10.15 and 15.22 m/s, respectively, for $T_g = 100°C$. These data for H = 1.5 m are marked in Fig. 6. For v_g = 0.03 m/s, as shown in Fig. 8a, the design point of the ACGIH code falls in the regimes of *strong suction* and *encapsulation* for $T_g = 100°C$ and $T_g < 65.5°C$, respectively. For higher v_g, as shown in Fig. 8b–d, the ACGIH designs deteriorate and even fall into the regimes of *transition* or *dispersion*. This is because the *critical operation boundary* rises in v_s with the increase of the rising gas velocity v_g. The deterioration of the operation becomes even more serious when the open-surface tank width becomes smaller, e.g. H = 1.0 and 0.5 m, as shown in the last column of Table 1. Using $v_b = 3.1$ m/s does not seem necessary because it requires a much higher pull-flow velocity v_s in order to push the operation point into the *strong suction* regime. Using a v_b lower than 3.1 m/s and matching with a higher pull-flow velocity v_s may

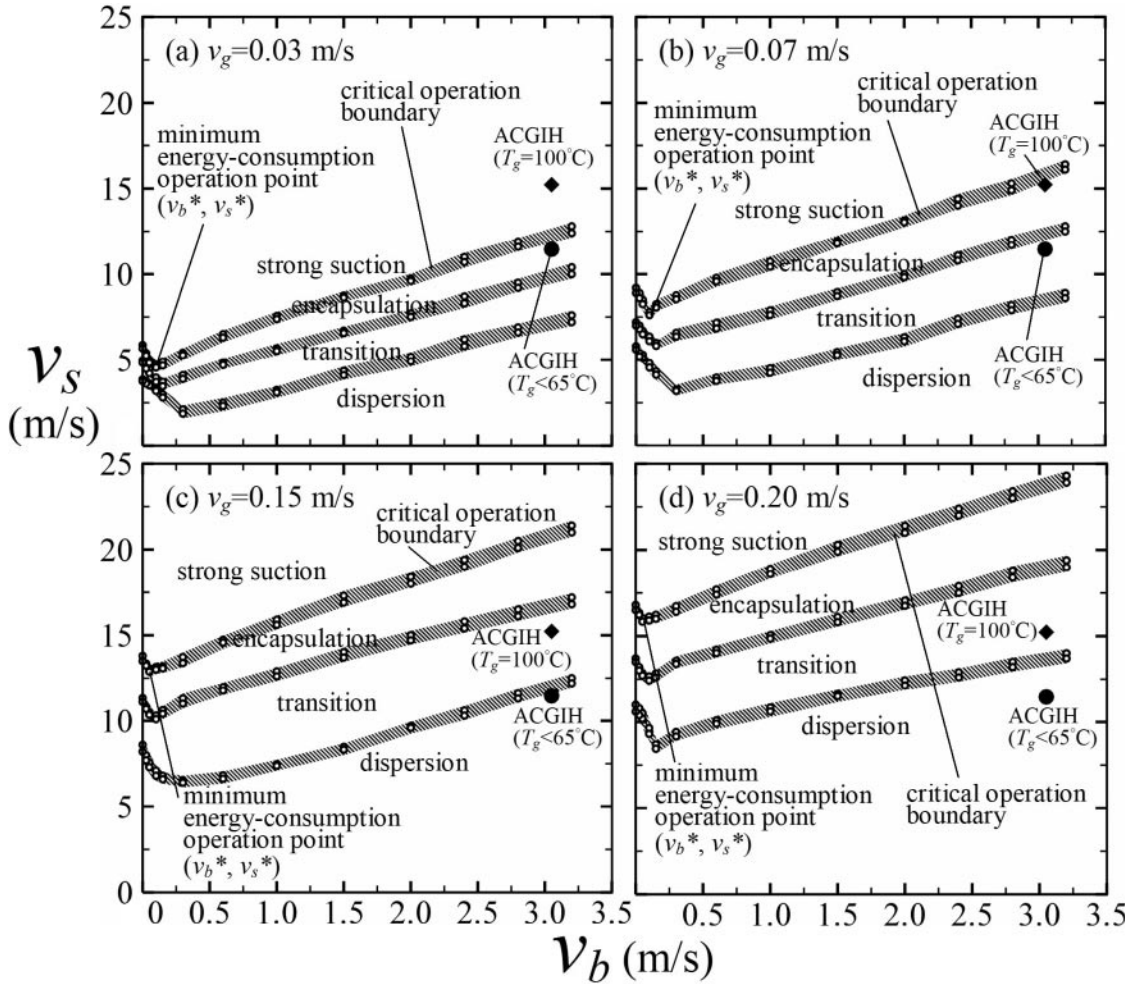

Fig. 8. Characteristic flow regimes at $H = 1.5$ m. (a) $v_g = 0.03$ m/s, (b) $v_g = 0.07$ m/s, (c) $v_g = 0.15$ m/s and (d) $v_g = 0.20$ m/s. Bands of short slashed lines represent boundaries between different characteristic flow modes.

be a better strategy to operate the system in the *strong suction* regime.

Equation (1) indicates that the push-flow rate Q_b is related solely to the size of the push nozzle. For a fixed nozzle width L, the push-flow rate Q_b is proportional to the square root of the nozzle height E. The push-jet velocity v_b therefore equals $40.9/E^{0.5}$. In other words, the push-nozzle height alone plays the role of determining the push-jet velocity. This design criterion does not seem logical because the effects of the pull velocity v_s, the rising gas velocity v_g, and the open-surface tank width H are not considered while determining push-jet velocity v_b.

Equation (2) implies that the pull-flow rate Q_s is a linear function of the open-surface tank area A_g with a proportionality coefficient of 22.9 m^3/min/°C for $T_g <$ 65.5°C. If the liquid-surface temperature T_g is greater than 65.5°C, then equation (3) takes the temperature effect (actually, it is the effect of the increased rising gas velocity) for consideration by adding a factor of $0.22T_g$ to the proportionality coefficient of 8.44 m^3/min/°C. The pull-flow velocity v_s is thus proportional to H/D. For a fixed pull-hood height D, it becomes that $v_s \propto H$. In other words, v_s is simply linearly proportional to H. In the next section on Design guidelines, we show that v_s is not a simple linear function of H. Instead, complex non-linear behaviors are embedded in these primary influential parameters v_b, v_s, v_g and H.

Design guidelines based on aerodynamic characteristics

Analysis. As discussed in the earlier section on Gas Transport Process and Aerodynamic Characteristics, it is preferred to operate the push–pull ventilation system in the regime of strong suction. The design work employing the aerodynamic observations would require determination of the functional relationship among the primary flow parameters of v_b, v_s, v_g and H

Table 1. Values of (v_b, v_s) calculated from ACGIH design code for H = 0.5–1.5 m, L = 0.5 m, E = 0.05 m

Tank width H (m)	T_g (°C)	v_b (m/s)	v_s (m/s)	Characteristic flow modes: v_g (m/s)
0.5	<65.5°C	3.10	3.82	Dispersion 0.05
				Dispersion 0.10
				Dispersion 0.15
	100°C		5.07	Transition 0.05
				Dispersion 0.10
				Dispersion 0.15
1.0	<65.5°C	3.10	7.63	Transition 0.05
				Dispersion 0.10
				Dispersion 0.15
	100°C		10.15	Encapsulation 0.05
				Transition 0.10
				Transition 0.15
1.5	<65.5°C	3.10	11.45	Encapsulation 0.05
				Transition 0.10
				Dispersion 0.15
	100°C		15.22	Strong suction 0.05
				Encapsulation 0.10
				Transition 0.15

on the critical operation boundary. The subsidiary geometric parameters, such as E, D, U and W, can be selected subsequently according to designers' experiences or the results of previous investigations. If the *critical operation boundaries* can be cast into a mathematical formula, determination of (v_b, v_s) for the operation of the system would be more convenient. By using all the experimental data of the critical *operation boundary* for various H's, Figs 9–11 are obtained for convenient access of the design procedure.

In Fig. 9, the normalized *minimum energy-consumption* suction velocity, v_s^*/v_g, of the pull hood at the *minimum energy-consumption point* increases non-linearly with the increase of H. This phenomenon is different from that implied by the ACGIH design code as shown in equations (2) and (3), which indicates that the design value of v_s should increase linearly with the increase of H. For a fixed H, the higher the rising gas velocity v_g is, the larger the value of v_s^*/v_g. The following regression equation provides for the convenience of calculation:

$$v_s^*/v_g = (-3362.3v_g^3 + 1893.9v_g^2 - 365.6v_g + 46.0) \times \exp[(-103.6v_g^3 + 38.6v_g^2 - 4.3v_g + 1.1) \times H] \quad (4)$$

where all variables adopt the metric units, i.e. v_s^*, v_g in meters per second and H in meters. Once the rising air velocity v_g is estimated and the open-surface tank width H is known, Fig. 9 or equation (4) can be employed to locate or to calculate the value of v_s^*. Maximum deviation of the fitted curve is 6.3% at H = 0.5 m and v_g = 0.15 m/s.

Figure 10 shows the variations of the normalized parameter v_s^*/v_b^* with the open-surface tank width H. Again, this variable v_s^*/v_b^* increases non-linearly with the increase of H. The following regression equation is provided for the convenience of calculation:

$$v_s^*/v_b^* = \exp[(-21.7v_g^2 + 6.7v_g + 1.1) \times H + (-53.4v_g^2 + 21.1v_g + 1.2)] \quad (5)$$

where all variables adopt the metric units, i.e. v_s^*, v_b^*, and v_g in meters per second and H in meters. Once the rising air velocity v_g is estimated, the open-surface tank width H is known, and the v_s^* is obtained by using Fig. 9 or equation (4), then Fig. 10 or equation (5) can be employed to locate or to calculate the value of v_b^*. Maximum deviation of the fitted curve is 11.2% at H = 0.5 m and v_g = 0.10 m/s.

The values of v_s on the *critical operation boundary* for $v_b > v_b^*$ can be taken approximately as a linear function of v_b, as shown in Fig. 8. The slopes S ($\equiv v_s/v_b$) of the *critical operation boundaries* for $v_b > v_b^*$ at various Hs and v_gs are collected in Fig. 11. It can be seen that the slopes of the *critical operation boundaries* at fixed H remain almost constant for different v_gs. The slope S, however, increases linearly

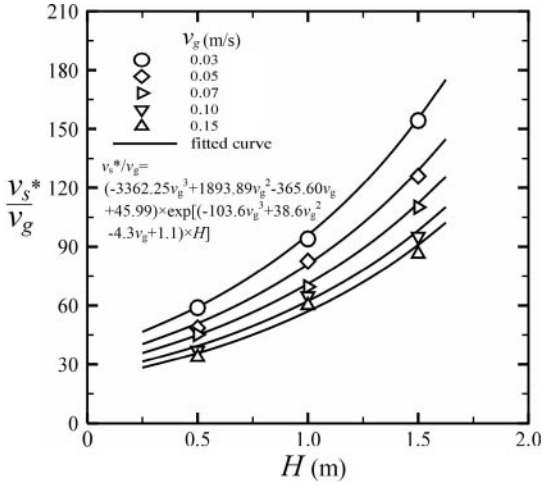

Fig. 9. Normalized minimum suction velocity, v_s^*/v_g, of pull hood at *minimum energy-consumption point*.

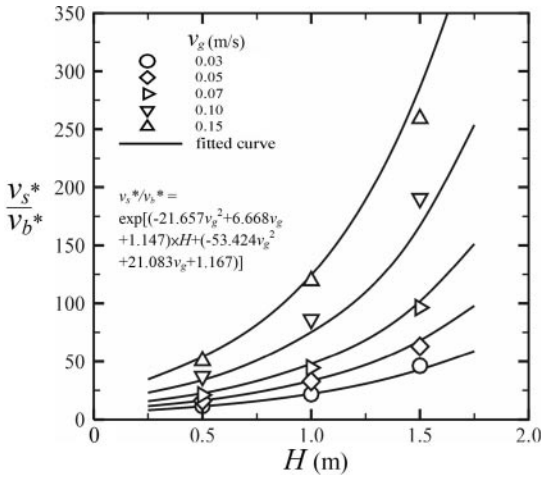

Fig. 10. Ratio between suction velocity and push velocity at *minimum energy-consumption point*.

with the increase of the open-surface tank width H. The linear equation is provided below for calculation:

$$S = 0.43H + 2.08 \tag{6}$$

where H is in m and S is dimensionless. Once the open-surface tank width H is known, the slope S can be obtained by using Fig. 11 or equation (6).

Once the values of (v_b^*, v_s^*) and S are obtained, the regime for the *strong suction* mode can be expressed by the following equation

$$v_s \geqslant v_s^* + S \times (v_b - v_b^*) \tag{7}$$

The equality holds on the *critical operation boundary*. A safety factor may be applied to v_s calculated on the critical operation boundary.

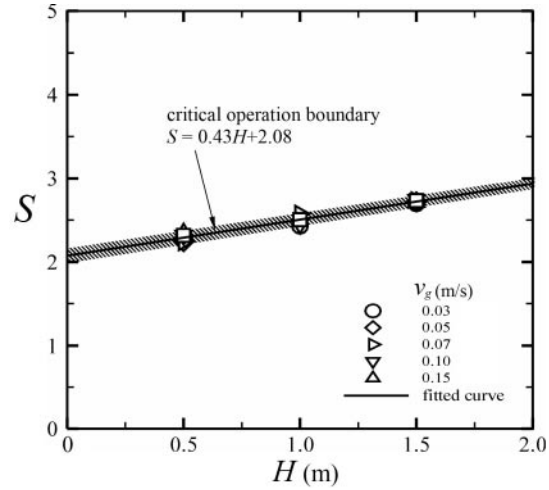

Fig. 11. Slopes of *critical operation boundaries*.

In our experience in practical applications, equations (4) –(7) can be confidently applied to the range of H smaller than 2.0 m. It is unknown if they would deviate to intolerable values when H is larger than 2 m.

Design guidelines. The design procedure for the primary parameters v_b, v_s, v_g and H, as discussed above, is summarized as follows:

1. For an open-surface tank with a width H, estimate possible maximum rising gas velocity v_g by employing thermodynamic principles or by measurements.
2. Based on the values of H and v_g, use equation (4) or Fig. 9 to obtain v_s^*.
3. Based on the values of H, v_g, and v_s^*, use equation (5) or Fig. 10 to obtain v_b^*.
4. Based on the values of H, use equation (6) or Fig. 11 to obtain the slope S.
5. Choose an operation push-jet velocity v_b. If the cross draft is not so serious, pick up a low value for v_b, e.g. taking $v_b = v_b^* \sim 1.0$ m/s for H which is shorter than 2 m. The smaller the H is, the lower the v_b should be taken. An excess v_b requires a large v_s to operate the system in the *strong suction* mode.
6. Based on the v_b predetermined in step (5) as well as the (v_b^*, v_s^*) and S calculated in steps (2)–(4), use equation (7) to calculate corresponding v_s on the *critical operation boundary*.
7. Multiply the value of v_s on the *critical operation boundary*, which is calculated in step (6), by a safety factor of ~1.1–1.2 to obtain the design value. This range of safety factor is obtained from the experience of the tracer gas concentration experiments.

8. Put guard plates along sides of the open-surface tank to avoid lateral leakage of the contaminants. The length of the guard plates is the same as the tank width H. The height can be as large as the height D of the pull hood. The purposes of the installation of guard plates are 2-fold. First, when the system is operated in the *strong suction* regime, the guard plates can reduce the lateral dispersion (leakage) of the contaminants and the influence of the lateral draughts because the contaminants are completely enclosed by the upper 'air curtain' and the side guard-plates under the operation condition of the *strong suction*. Second, the push-jet velocity v_b can be set at low value so that energy consumption can remain low.

Some of the authors' experiences to design the subsidiary geometric parameters, E, D, U and W, are provided as follows.

1. The height of the push nozzle, E, can be designed as a value between 2 and 5 cm, depending on the seriousness of the cross-draft around the push–pull system. If the cross-draft is large, a larger value of push-nozzle height can be considered in order to increase the 'bulk-momentum' of the isolation air curtain. For E smaller than 1 cm, the pressure drop becomes large.
2. The height of the pull hood D can be taken in the range of $1 \leqslant D/E \leqslant 2$. In the authors' experience, taking $D/E = 2$ is of little help in lowering the level of the *critical operation boundary* than taking $D/E = 1$. This arrangement may lower a little the necessity of the critical suction velocity v_s.
3. The depth between the pollutant emission surface and the lower edge of the pull hood, i.e. U, can be determined according to Shibata *et al.*'s (1982b) suggestions: $U/D \geqslant 2$.
4. Aerodynamically, the suction-hood flange would not be necessary if the push–pull system is operated in the *strong suction* mode because the push jet and the entrained pollutants and atmosphere air would not disperse by convection to the area higher than the upper edge of the pull hood. However, installation of a short flange may be helpful to reduce extra energy consumption induced by the flows turning-around from the upper region of the suction hood.

SF_6 tracer gas validation

In order to validate the effectiveness of the proposed design guidelines, tracer gas concentration experiments for measurement of the capture efficiency are conducted. When measuring the capture efficiency of the push–pull system, the sulfur hexafluoride gas of a certain flow rate is first injected into the pull hood. After evolving along a exhaust pipe 10 m long for good mixing, the concentration of the SF_6 tracer gas, which is denoted as $C_{o,s}$, is measured in the exhaust at the location ~0.5 m upstream of the end-opening of the exhaust pipe. The sulfur hexafluoride gas of the same flow rate as used in the measurement of $C_{o,s}$ is injected into the inlet piping that is connected the open-surface tank and is released with the rising air. Again, the SF_6 tracer gas concentration is measured at the point ~0.5 m upstream of the end-opening of the pipe and is denoted by $C_{o,g}$. The capture efficiency η is defined as the quotient of $C_{o,g}$ divided by $C_{o,s}$, i.e. $\eta \equiv C_{o,g}/C_{o,s}$.

Figure 12 shows the capture efficiency measured for $H = 1.0$ at $v_g = 0.05$ and 0.15 m/s. Figure 12a,b shows the case without guard-plates. Figure 12c,d presents the case with guard-plates installed. Figures for $H = 0.5$ and 1.5 m at $v_g = 0.03$, 0.10 and 0.20 m/s are not shown here because their characteristics are similar to Fig. 12. In the system either without guard-plates or with guard-plates installed, the capture efficiency η increases with the increase of the pull velocity v_s. In the regime of the *dispersion* mode, the capture efficiency is low and the increase rate is high. In the *strong suction* regime, the capture efficiency is generally increased to values approximately higher than 98%. When Fig. 12c and d are compared with Fig. 12a and b, the capture efficiencies of the push–pull system with guard-plates is obviously higher than those without guard-plates. In order to attain a capture efficiency higher than 99%, it requires the critical value of v_s corresponding to a certain v_b on the *critical operation boundary* to be raised by ~10~20%.

The capture efficiencies measured in the cases of the operation conditions set according to the ACGIH design code, i.e. $(v_b, v_s) = (3.05, 7.63)$ m/s are marked in Fig. 12 for comparison. Although ACGIH did not suggest the installation of guard-plates, the benefit is apparent by doing so. At $v_g = 0.05$ m/s, the capture efficiencies of the ACGIH design fall in the *transition* regime. In this case, it is medium high to about 97 and 98% for no guard-plates and guard-plates installed, respectively, as shown in Fig. 12a and c. To attain the same capture efficiency as that of the ACGIH design, the energy consumption required using the present design method is much lower than the conventional ACGIH method. For instance, the capture efficiency shown in Fig. 12c is about 98% by setting $(v_b, v_s) = (3.05, 7.63)$ m/s using the ACGIH design code. Lower velocity pairs of $(v_b, v_s) = (1.0, 5.6)$ m/s is good enough to attain the same capture efficiency if the current design method is employed. If the velocity pair $(v_b, v_s) = (1.0, 8.0)$m/s is adopted, the operation point falls in the *strong suction* regime and the capture efficiency can even attain almost 100%. Obviously, an over-blowing by the push nozzle is the primary cause of downgrading the operation characteristic flow mode. This phenomenon can be

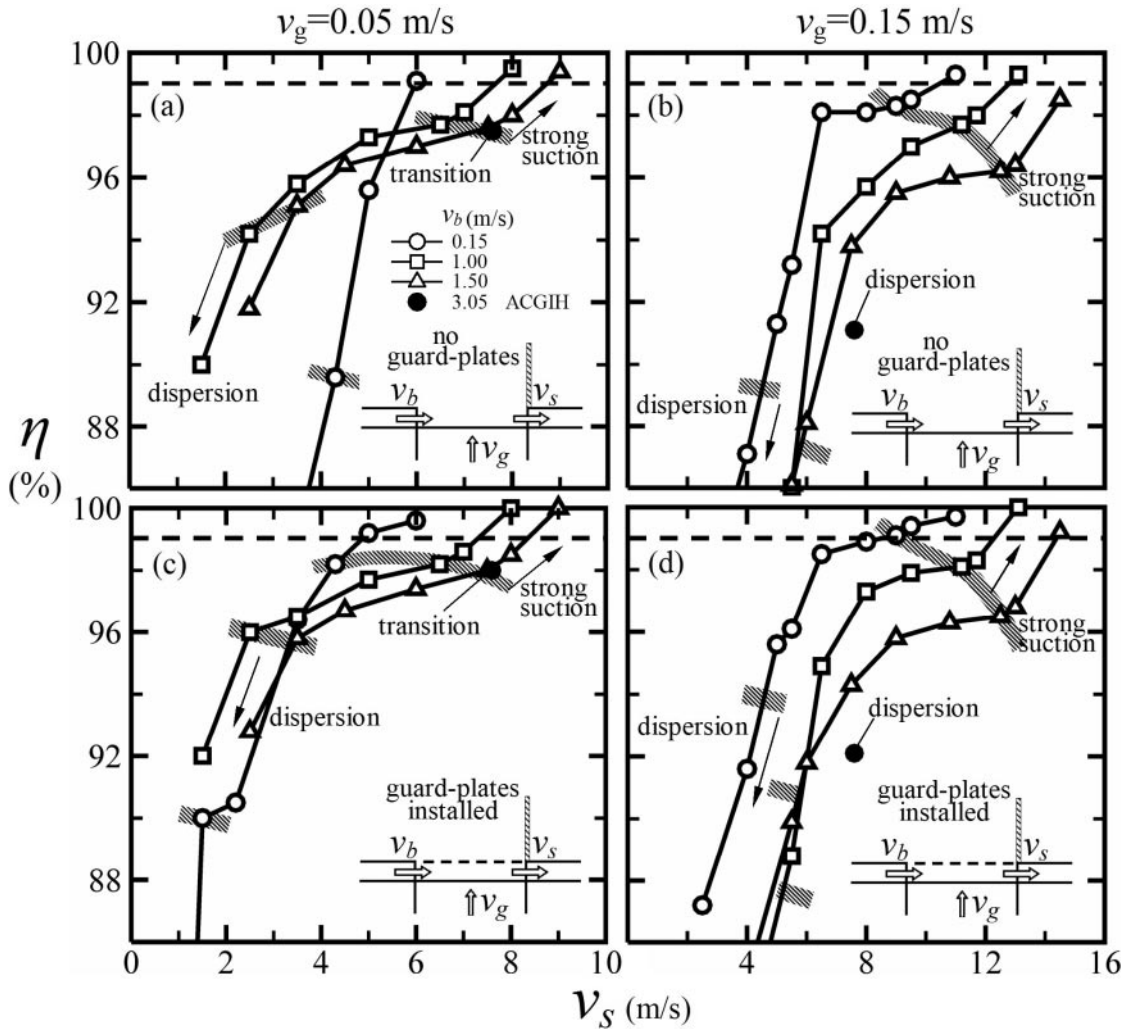

Fig. 12. Capture efficiency η measured for H = 1.0 at (a,c) v_g = 0.05 and (b,d) v_g = 0.15 m/s.

observed more clearly in the following example. At v_g = 0.15 m/s, as shown in Fig. 12b,d, the capture efficiencies measured for the ACGIH designs are low because the operation points, i.e. (v_b, v_s) = (3.05, 7.63) m/s, fall in the *dispersion* regime. If the push velocity v_b is reduced from 3.05 to 0.15 m/s and the pull velocity v_s is kept at the same value of 7.63 m/s, the capture efficiency would be increased to about 99%, as shown in Fig. 12d.

CONCLUSIONS

The flow patterns and aerodynamic characteristics of the push–pull ventilation system were phenomenologically and quantitatively studied. The following conclusions are drawn from the results and discussion.

1. Four characteristic flow modes, *dispersion*, *transition*, *encapsulation* and *strong suction*, can be identified in different regimes in domain of the push-jet velocity and the pull-flow velocity, according to the aerodynamic characteristics diagnosed by flow visualization and laser Doppler velocimetry. To obtain better capture efficiency, operating the push–pull system in the *strong suction* regime with the assistance of guard-plates is a better strategy than operating in other characteristic regimes.
2. By operating the push–pull system on the *critical operation boundary*, a capture efficiency of higher than ~98% is possible if the guard-plates are installed. The capture efficiency can be further increased to higher than 99% if the *critical pull velocity* is increased by 10–20%. When the obstacle objects exist in the pathway of the push–pull flow, the present results may require some modifications.
3. The proposed design guidelines suggest a step-by-step procedure for designers to determine the

primary flow parameters, the push-jet velocity and the pull-flow velocity, if based on the open-surface tank width and estimated rising gas velocity. The design ranges of the subsidiary geometric parameters, such as the push-nozzle height, pull-hood height, distance between the pull hood and the free surface and the push-hood flange, are suggested according to the authors' experiences.

4. The push–pull system by using the ACGIH design criteria can be further refined in both capture efficiency and energy consumption by considering the aerodynamic characteristics of the flow transport phenomena.

Acknowledgement—This research was supported by the Institute of Occupational Safety and Health, Council of Labor Affairs of Taiwan, PRC.

REFERENCES

ACGIH. (2001) Common industrial ventilation. Industrial ventilation—A manual of recommended practice. 24th edn. American Conference of Governmental Industrial Hygienists. Lansing, MI, pp. 10-108–10-112.

Flagan RC, Seinfeld JH. (1988) Fundamentals of air pollution engineering. Englewood Cliffs, NJ: Prentice Hall, pp. 290–357.

Malin BS. (1945) Practical pointers on industrial exhaust system. Heat Vent; 42: 75–82.

Marzal F, González E, Miñana A *et al*. (2002a) Analytical model for evaluating lateral efficiencies in surface treatment tanks. Am Ind Hyg Assoc J; 63: 572–7.

Marzal F, González E, Miñana A *et al*. (2002b) Determination and interpretation of total and transversal linear efficiencies in push–pull ventilation systems for open surface tanks. Ann Occup Hyg; 46: 629–35.

Marzal F, González E, Miñana A *et al*. (2002c) Influence of push element geometry on the capture efficiency of push–pull ventilation systems in surface treatement tanks. Ann Occup Hyg; 46: 383–93.

Marzal F, González E, Miñana A *et al*. (2003a) Methodologies for determining capture efficiencies in surface treatment tanks. Am Ind Hyg Assoc J; 64: 604–8.

Marzal F, González E, Miñana A *et al*. (2003b) Visualization of airflows in push–pull ventilation systems applied to surface treatment tanks. Am Ind Hyg Assoc J; 64: 455–60.

Newman BG. (1961) The deflection of plane jets by adjacent boundaries—Coanda effect. In Lachmann GV, editor. Boundary layer and flow control—its principles and application. Vol. 1. New York: Pergamon Press, pp. 232–64.

Rota R, Nano G, Canossa L. (2001) Design guidelines for push–pull ventilation systems through computational fluid dynamics modeling. Am Ind Hyg Assoc J; 62: 141–8.

Shibata M, Howell RH, Hayashi. (1982a) Characteristics and design method for push–pull hoods: Part 1—cooperation theory on airflow. ASHRAE Trans; 88: 535–56.

Shibata M, Howell RH, Hayashi. (1982b) Characteristics and design method for push–pull hoods: Part 2—streamline analyses of push–pull flows. ASHRAE Trans; 88: 557–70.

Tritton DJ. (1988) Physical fluid flows, 2nd edn. New York: Oxford University Press, pp. 289–94.